Exp Fluids (2015) 56:168
DOI 10.1007/s00348-015-2035-2

RESEARCH ARTICLE

The effects of initial conditions and circulation deposition on the inclined-interface reshocked Richtmyer–Meshkov instability

David Reilly[1] · Jacob McFarland[2] · Mohammad Mohaghar[1] · Devesh Ranjan[1]

Received: 21 April 2015 / Revised: 10 July 2015 / Accepted: 24 July 2015 / Published online: 11 August 2015

Abstract An experimental study of a twice-accelerated Richtmyer–Meshkov instability, where reshock provides the second acceleration, focusing on the effects of initial conditions and circulation deposition is presented. Experiments were performed using the inclined shock tube facility at the Shock Tube and Advanced Mixing Laboratory. Three experimental cases are presented that have the same Atwood number, inclination angle, and Mach number, but are differentiated by their pre-reshock development time. Both Mie scattering and particle image velocimetry diagnostics were implemented. Velocity statistics were ensemble-averaged over instantaneous realizations for each case before and after reshock. Results show that while the mix width decreases after reshock, the interface length continues to increase because the reshock wave amplifies small-scale perturbations on the pre-reshock interface, resulting in greater mixing. A more developed interface also experiences greater circulation deposition after reshock. After reshock, the sign of the vorticity near the interface reverses due to a second application of baroclinic torque by the reshock wave. Velocity statistics showed that the cross-correlation ($\overline{u'v'}$) is nonzero over much of the mixing layer, which indicates that shear and anisotropy are present. Turbulent kinetic energy spectra for the most developed case after reshock exhibited a $k^{-5/3}$ inertial range.

✉ Devesh Ranjan
devesh.ranjan@me.gatech.edu

[1] George W. Woodruff School of Mechanical Engineering, Georgia Institute of Technology, 801 Ferst Drive, Atlanta, GA 30332, USA

[2] Department of Mechanical and Aerospace Engineering, University of Missouri, E2412 Lafferre Hall, Columbia, MO 65211, USA

1 Introduction

The Richtmyer–Meshkov instability (RMI) (Richtmyer 1960; Meshkov 1969) is a hydrodynamic instability that results from the interaction of misaligned pressure and density gradients. The pressure gradient required is introduced through a shock wave that interacts with a density gradient in the form of an interface between fluids of different densities. The shock-interface interaction causes vorticity to be generated through the baroclinic term of the vorticity equation, $D\vec{\omega}/Dt = \left[\frac{1}{\rho^2}\vec{\nabla}\rho \times \vec{\nabla}P\right]$, where $\vec{\omega}$ is the vorticity, $D\vec{\omega}/Dt$ is the substantial derivative of $\vec{\omega}$, ρ is the density, and P is the pressure. The magnitude of the baroclinic term of the vorticity equation is based on the strength of the pressure and density gradients and the angle of misalignment between them at the time of interaction. Two non-dimensional quantities, the Mach number and the Atwood number, are used to describe the strength of the pressure and density gradients, respectively. The Mach number ($M = W/c$) is a ratio of the shock wave speed to the speed of sound in the medium. The Atwood number is defined as $A = \frac{\rho_h - \rho_l}{\rho_h + \rho_l}$, where the subscripts h and l denote the heavy and light fluids, respectively, for the light-over-heavy case.

The motivation behind many current research efforts into the RMI is its effect on the development of inertial confinement fusion (ICF) (Kramer et al. 2009). During the compression stage of the ICF process, the less dense ablation layer on the more dense fuel pellet creates a density gradient that is impacted by a shock wave created by the high-powered laser, introducing a pressure gradient into the system. This interaction causes the RMI to mix the fuel and coating which reduces the efficiency and therefore the energy output of ICF.

The RMI has been studied in depth both experimentally and computationally beginning with the seminal works of Richtmyer (1960) and Meshkov (1969). This hydrodynamic instability was actually pre-discovered by Jahn (1956) who experimentally studied the refraction of plane shock waves using an oblique density interface. However, the focus of author's work was on the physics of shock-refraction and boundary layer development, and not the hydrodynamic instability developing on the gaseous interface. The pressure gradient has been created in many fashions experimentally, including accelerating the experimental facility as a whole (Chapman and Jacobs 2006) or as is the case for the work presented in this paper, a shock tube is used. In a shock tube, a high-pressure volume (the driver) is separated from a low-pressure volume by a thin diaphragm. The diaphragm is then ruptured causing compression waves to travel into the low-pressure volume which will coalesce into a planar shock wave given sufficient length. The method used to create the density gradient within a shock tube is dependent on the facility. In some facilities, where the orientation of the gases is unstable, a membrane is used to maintain the desired density gradient (Vetter and Sturtevant 1995; Smith et al. 2001). In other facilities, the arrangement of the gases allows gravity to maintain the interface, whether it is planar (Jones and Jacobs 1997) or a vertical, circular column (Olmstead et al. 2015; Wayne et al. 2015). A similar technique was employed in this facility. The facility used is not vertical; rather, it is inclined which allows for a repeatable, non-perpendicular planar interface (McFarland et al. 2014). Computational studies of the RMI have been performed using many different methods including large-eddy simulations (Hill et al. 2006), weighted essentially non-oscillatory simulations (Latini et al. 2007; Schilling et al. 2007; Schilling and Latini 2010), and simulations performed with an arbitrary Lagrangian–Eulerian hydrodynamics code (McFarland et al. 2011, 2014; Morgan et al. 2012). Simulations of the RMI are currently expensive and will continue to stress computing resources as higher resolutions are desired and more complex models are produced.

A shock tube with a closed end gives the ability to shock an evolving RMI interface a second time utilizing the shock reflection from the end wall. This process is called reshock which is important in ICF and has also been studied experimentally and computationally (Schilling et al. 2007). In the case of Vetter and Sturtevant (1995), a horizontal shock tube was used to determine the effect of reshock on the turbulent mixing zone created by the RMI. They found that although the thin membrane used to form the interface plane had a significant influence on the initial growth rate of the interface, it had little effect on growth rates after the first reflected shock. In work that was similar to that of Vetter and Sturtevant, Leinov et al. (2009) also studied the effect of reshock on the turbulent mixing zone in a horizontal shock tube. Leinov et al. also varied the distance and material of the end wall to observe the effects of different reshock strengths and interaction times and compared the results to numerical simulations they performed. Balakumar et al. (2008) studied the effect of reshock on the structures of a sinusoidal gas curtain interface. Numerical simulations have also been performed for the initial condition used in this work (the inclined-interface) by Samtaney and Zabusky (1993), from which they developed a circulation model. McFarland et al. (2011) also studied the inclined-interface RMI after reshock using ARES hydrodynamic code with adaptive mesh refinement (AMR). This study found that despite disparate initial conditions, the linear and nonlinear cases studied showed similar mix widths after reshock.

The goal of this paper is to investigate the effects of reshock interaction time and vortex scales and distribution on the development of the inclined-interface Richtmyer–Meshkov instability. Section 2 will describe the experimental facility and the configuration used for the experiments. The developing interface of the inclined-interface RMI will be reshocked at three different stages of development, each with a different level of vortex scales and distribution. The results are given in Sect. 3. A qualitative study will be presented through high temporal resolution Mie scattering images. Mixing width and interface length will be measured from the Mie scattering images to determine the interface growth rate, and particle image velocimetry will be used to map the velocity of the flow to generate vorticity fields and circulation data for a qualitative comparison. The Kolmogorov scale and Taylor microscale for the experimental cases will be calculated and used to analyze the turbulent kinetic energy spectra for each case. Finally, the turbulent kinetic energy spectra will be ensemble-averaged and normalized, and compared between the experimental cases.

2 Experimental facility

2.1 Facility overview

The experiments were performed in the shock tube at the Shock Tube and Advanced Mixing Laboratory, and a brief overview of the experimental facility will be presented. A more in-depth description of the facility can be found in McFarland et al. (2014). The shock tube facility utilizes a variable inclination design to create a repeatable inclined-interface initial condition for performing RMI experiments. The shock tube is 8.6 m in length and is functional at all angles from horizontal (0°) to vertical (90°). The shock tube was designed to be modular to allow for multiple experimental

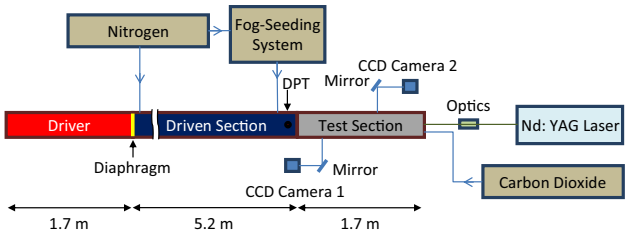

Fig. 1 Schematic of the experimental facility

options and can sustain shock strengths up to Mach 3.0 into atmospheric air. Following the driven section is a modular test section that allows for imaging at multiple locations at once and overlapping images for situations when the interface grows beyond the scope of a single window. The test section also contains multiple locations where a fluid interface can be created, an ability that features prominently in the present experiments. A schematic of the facility is shown in Fig. 1.

Diagnostic hardware employed in conjunction with the facility allows for a wide variety of data to be acquired from the experiments. Vital to the timing of the other diagnostics, dynamic pressure transducers are located in the driven section, test section, and on the end wall of the shock tube. The pressure transducers in the driven section allow for the initial shock speed to be calculated using the difference in rise times and the distance between the transducers. The rise time of the last dynamic pressure transducer is used to trigger the flow visualization system. The flow visualization system consists of two TSI Inc. PowerView Plus 2 MP cameras designed for particle image velocimetry (PIV) that are also capable of capturing Mie scattering images and a dual cavity New Wave Research Gemini PIV laser capable of providing 200 mJ per pulse at 532 nm. The seeding required for the PIV and Mie scattering techniques is provided by a Pea Soup fog machine. Fog particles are introduced into the light fluid through a port close to the test section only when employing Mie scattering, but are introduced into both the light and heavy gases for PIV studies. The UK Atomic Energy Authority measured the size of the fog particles using a Laser Doppler Anemometer and found the mean particle size to be 0.2 μm in diameter (a detailed description of the particle sizing procedure can be found in the AEA Working Instructions 1998). In the case of the heavy gas, the fog particles are introduced through a bypass in the heavy gas fill line. Images are captured using TSI INSIGHT^{TM} 4G software, and PIV vectors are computed using built-in processing capabilities.

2.2 Experimental cases

The experimental cases presented here are defined by a single Mach number ($M = 1.55$), angle of inclination ($\theta = 60°$), pre-shock Atwood number ($A \cong 0.23$), and amplitude-to-wavelength ratio ($\eta/\lambda \cong 0.29$). An Atwood number of 0.23 for the three cases is achieved by using nitrogen as the light gas and carbon dioxide as the heavy gas. These common factors allow us to focus on the effect of interface development on circulation by varying the interaction time of the reshock wave. By utilizing the modular nature of the shock tube test section, it was possible to create the initial interface at three different distances from the bottom wall of the shock tube (other distances could be created if desired). These distances define Cases 1, 2, and 3, respectively, and correspond to approximate reshock interaction times shown in Table 1.

Table 1 Definition of experimental cases

	Case 1	Case 2	Case 3
IC to bottom wall	0.52 m	1.07 m	1.61 m
Development time	1.64 ms	3.50 ms	5.11 ms

The different interface creation distances and reshock interaction times allow for different development times for each case. The effects of these development times on the RMI will be explored in the following sections. The development of the pre-reshock interface is shown in relation to the development caused by the initial shock in Fig. 2.

Figure 3 shows x-t plots for the three experimental cases presented in this work. Annotated on the plots is the triggering dynamic pressure transducer location as well as the bounds of the visualization area used to capture the reshock data. Evident from the contours representing the expansion waves from the reshock wave interaction with the interface, the time that the reshock of the RMI can be studied is limited by the time until the expansion waves interact with the interface. The different reshock development times for the cases are directly related to the distance from the interface to the bottom wall of the shock tube. As the distance from the bottom wall increases, the velocity difference between the transmitted shock and the interface generates a larger gap before the transmitted shock reflects from the bottom wall.

3 Results

3.1 Qualitative results

Qualitative Mie scattering images were obtained for each of the three cases. All of the images were processed to remove background noise and vertical lines created by discontinuities in the wall facing the camera. Furthermore, the contrast between the region of unseeded CO_2 and the seeded N_2 was enhanced. The full-field view of the acquired Mie scattering images are presented in this section without cropping

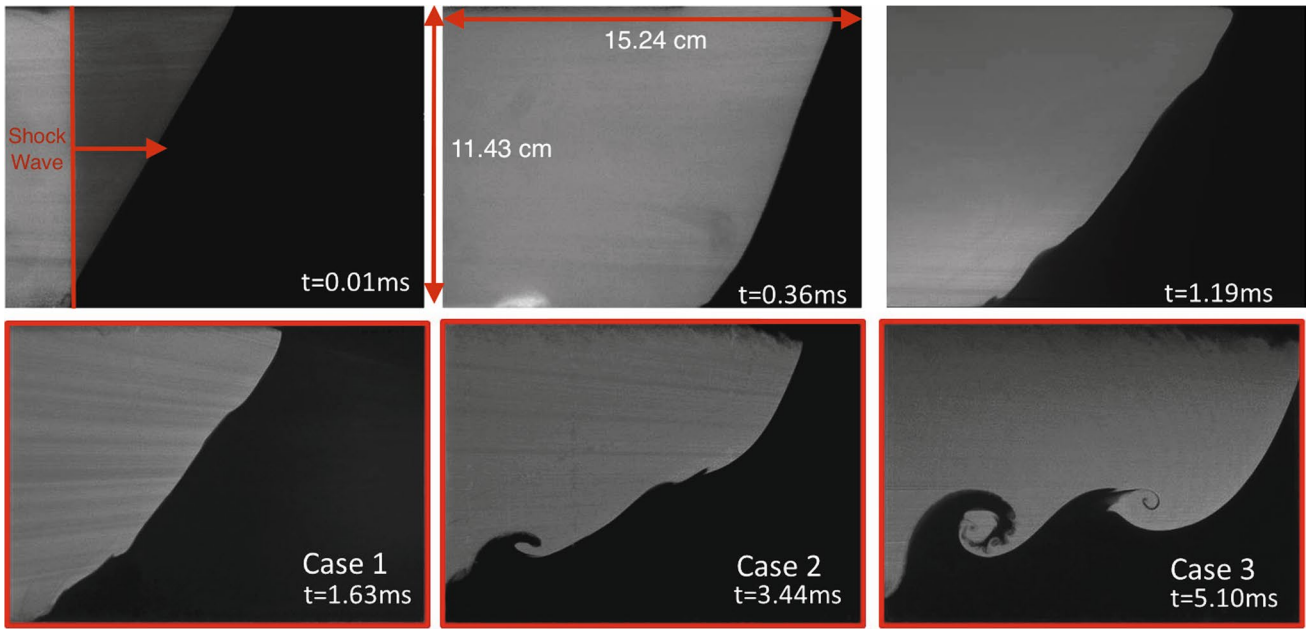

Fig. 2 Initial interface shock development of inclined-interface RMI for Mach number 1.55, Atwood number 0.23, and angle of inclination 60°

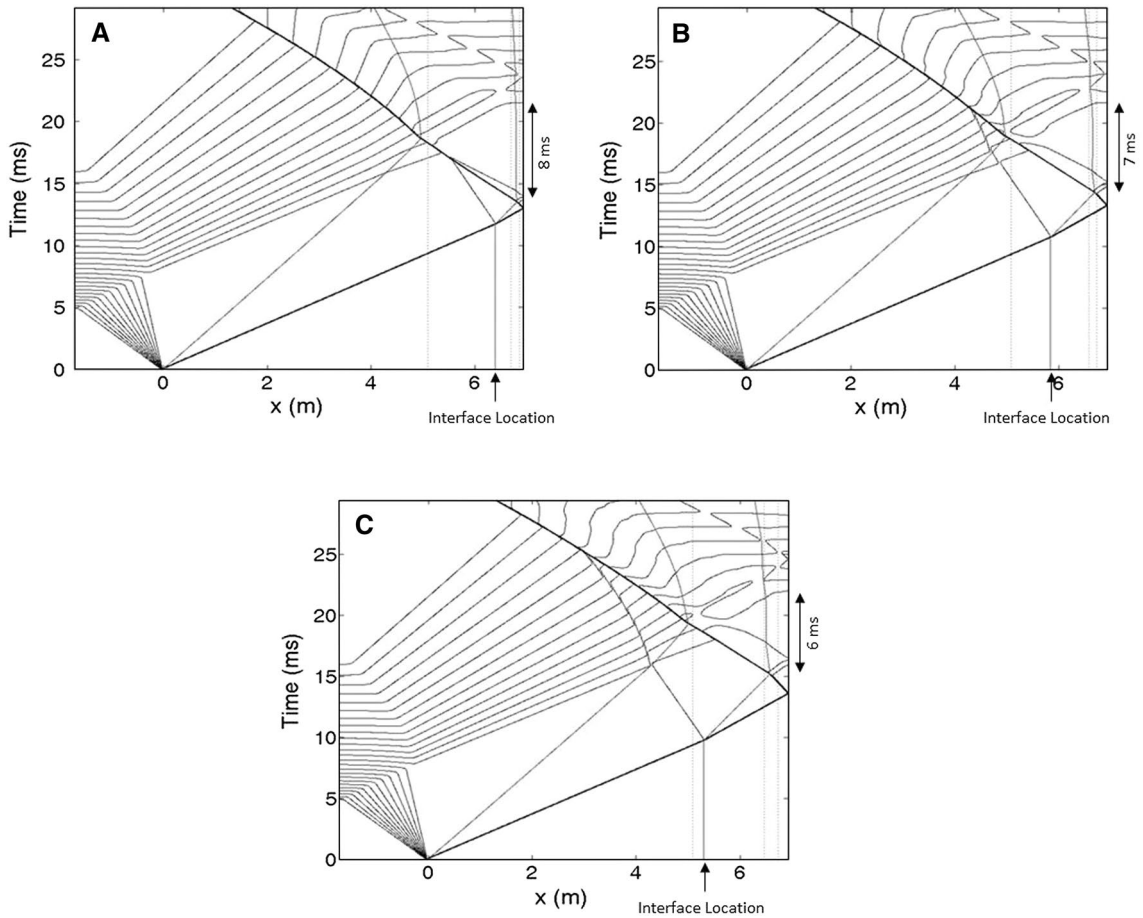

Fig. 3 *x–t* plots for Case 1 (**a**), Case 2 (**b**), and Case 3 (**c**) with dynamic pressure transducer and window locations annotated

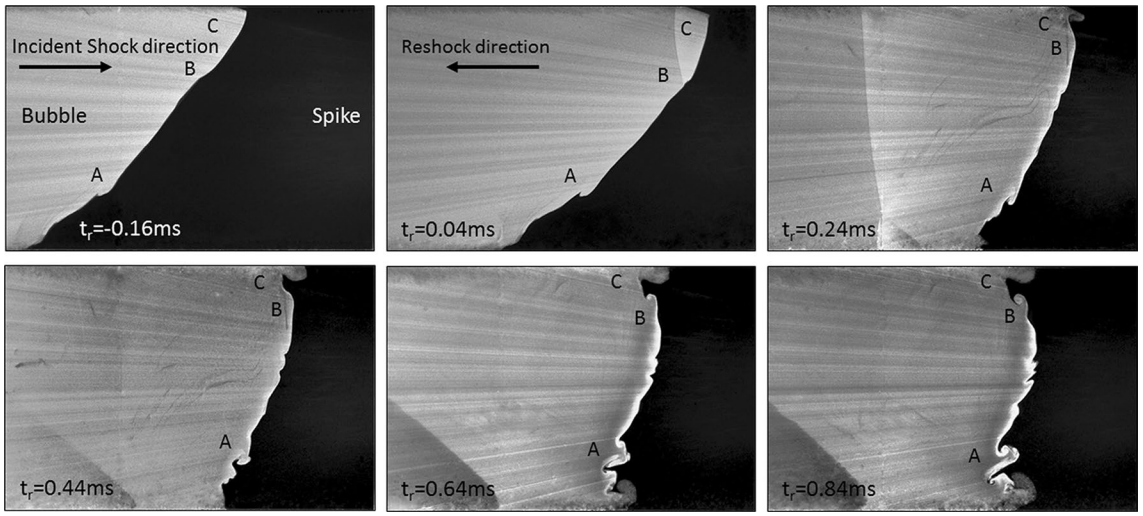

Fig. 4 Case 1 Mie scattering image time series with interface 0.52 m from the end wall

the boundary layers visible near the side walls. In Case 3, the interface stretched to the point that overlapping windows were required to capture the whole flow field featuring the interface. When this occurred, the images from two cameras were combined to make a single image. A discussion of the RMI before reshock is presented in previous work of McFarland et al. (2014).

The first time series of Mie scattering images (Fig. 4) are for Case 1 where the interface was 0.52 m from the shock tube end wall. The primary and secondary vortices have not yet formed in the first time step and appear as inflection points labeled A and B. These inflection points stretch and rotate clockwise as time progresses through 0.84 ms. At 0.04 ms, the shock wave can be seen as a sharp line dividing bright and less bright fog near the bubble tip labeled C. The shock wave is curved due to a mismatch in acoustic impedance (ρc) between N_2 and CO_2. The mismatch also causes a phase inversion as the interface compresses causing it to appear to rotate counterclockwise. A dark, triangular region forms at 0.24 ms and remains visible through late times. This is caused by a slip line formed by a lambda shock created by the refraction of the reshock wave through the interface. The problem of a refracted shock wave through a slow-fast interface has been thoroughly studied both theoretically and experimentally using Schlieren photography by Abd-El-Fattah et al. (1976) and Abd-El-Fattah and Henderson (1978a, b). The authors found that the slow-fast phenomenon could be categorized into three groups based on inverse strength and incident shock. Also of interest is a halo on the twice-shocked interface, most visible at 0.84 ms. This halo may result from an index of refraction mismatch at the interface, which translates into a markedly strong Mie scattering signal.

Figure 5 shows the time series of Mie scattering images for Case 2 where the interface was 1.07 m from the shock tube end wall. The primary vortex labeled A shows more development at −0.06 ms compared to Case 1. The primary vortex is compressed during the compression caused by the reshock wave passing through the interface at 0.34 ms. The acoustic impedance mismatch again causes a phase inversion in the interface during the compression phase similar to what is seen in Case 1. The inflection at B becomes amplified after reshock and forms a pronounced protrusion from the interface by 0.94 ms. Similarly, the bubble tip labeled C protrudes out from the interface, thereby increasing the area over which mixing may occur. Large structures remain stagnant at late times as small-scale development ensues.

The final set of Mie scattering images (Fig. 6) is for Case 3 where the interface was 1.61 m from the shock tube end wall. In the first image, the primary vortex labeled A shows several smaller, fractal-like Kelvin–Helmholtz rollups which have been observed by Peng et al. (2003) and result in increased vorticity deposition as well as a transition to turbulence. The well-developed vortices are compressed after the reshock at 0.33 ms resulting in increased mixing at small scales at late times. As in Cases 1 and 2, the bubble tip at C protrudes from the interface leading to additional area over which mixing may occur.

3.2 Quantitative results

3.2.1 Mixing width data

The Mie scattering images provide an estimate of the mixing at the interface by calculating the mixing width, as shown schematically in Fig. 7, which is created for

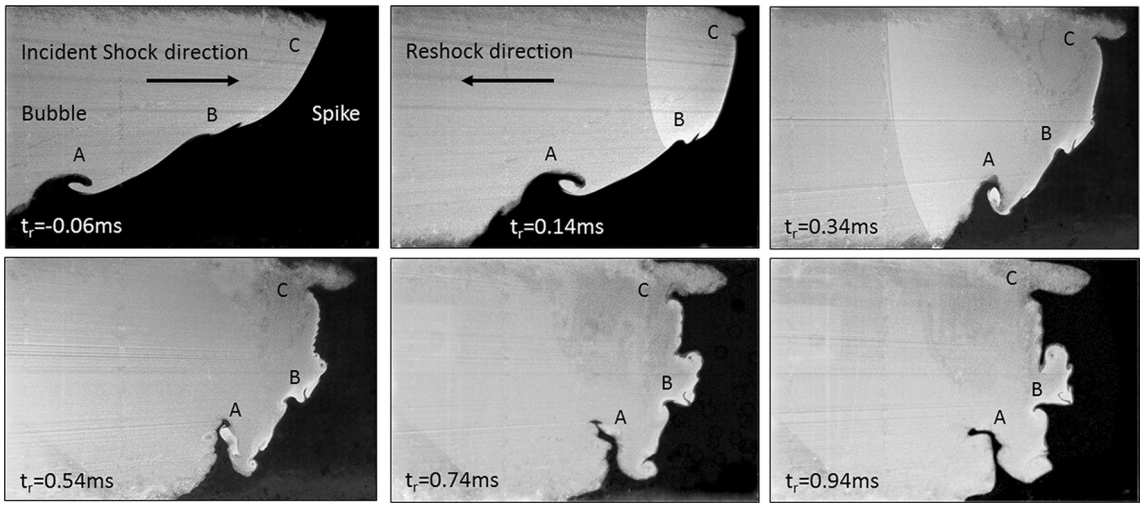

Fig. 5 Case 2 Mie scattering image time series with interface 1.07 m from the end wall

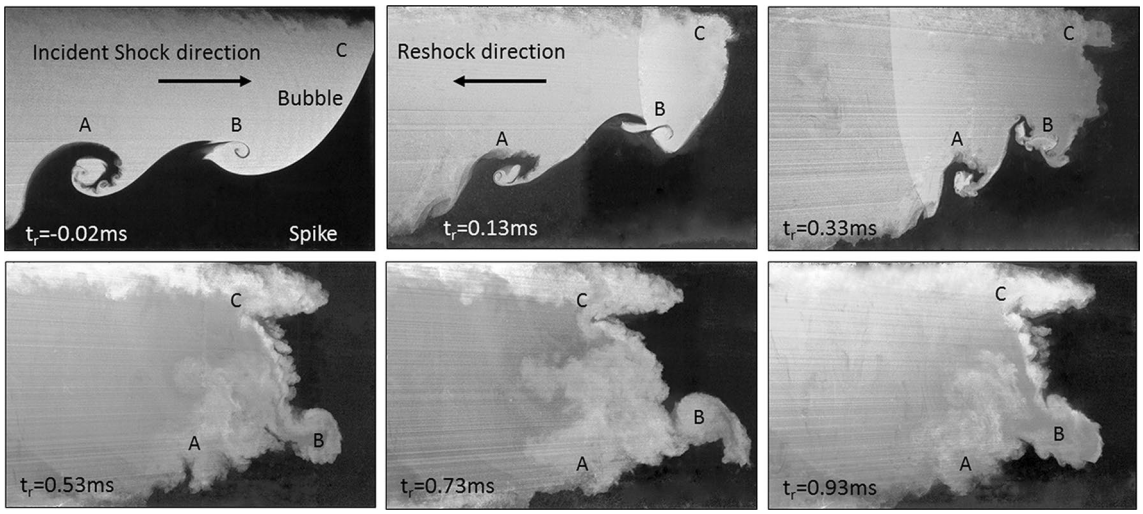

Fig. 6 Case 3 Mie scattering image time series with interface 1.61 m from the end wall

illustrative purposes and is not intended to represent the exact interface evolution. To calculate the mixing width, the boundary layers are cropped, and the image is converted into a binary image using an intensity threshold. The intensity threshold is the pixel intensity below which a pixel will be changed to zero and above which it will be converted to one. The threshold was chosen to accurately represent the fluid interface. Once the image is purely black and white, the columns of pixels where the image is 5 and 95 % white are determined starting from the edge of the image inward, and the pixel distance between the columns is recorded. The pixel distance is converted into a dimensional distance using the calibration image. The mixing width measurements for the images in the three experimental cases are presented with data from initial shock development in Fig. 8. The mixing width data are used to calculate the mixing width growth rate by applying a linear regression to the data points after reshock that follow a linear trend for all three cases. These growth rates, as shown in Table 2, show that the interface stretches during the initial development, but all three cases compress at similar rates post-reshock. It is clear from Figs. 5 and 6 that the similar compression rates after reshock are due to phase inversion, which occurs at a similar rate in each case.

3.2.2 *Interface length data*

The Mie scattering images can also be used to measure the interface length. To measure the interface length, the image is filtered with a median filter to reduce noisy gradients,

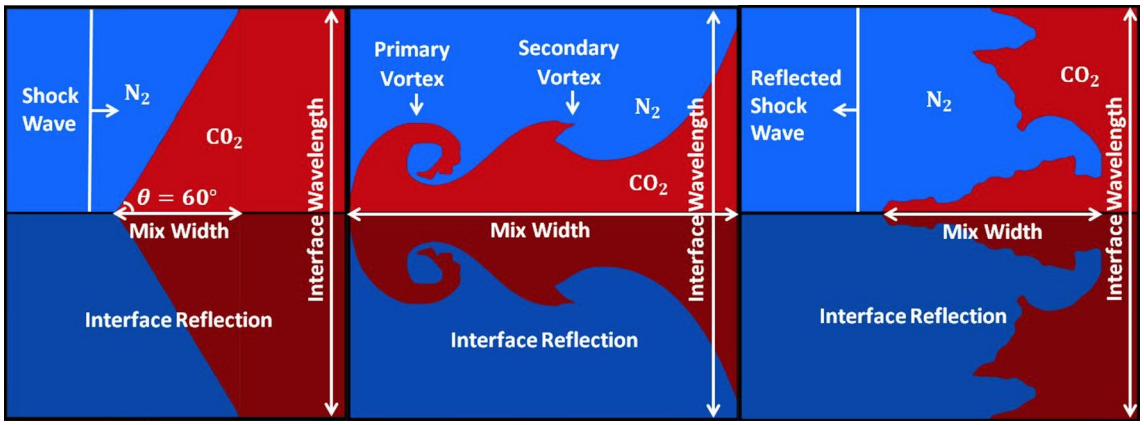

Fig. 7 Schematic showing inclined-interface mixing width and wavelength with interface reflection

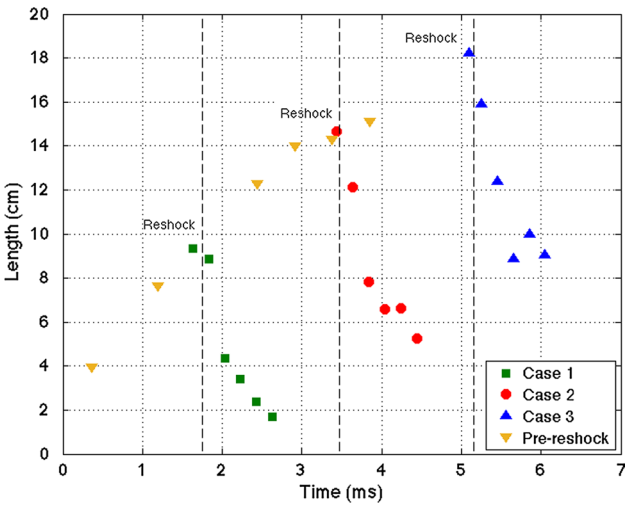

Fig. 8 Mixing width data for Cases 1, 2, and 3

and then the image is analyzed in the streamwise direction to find the sharpest gradient within one pixel of the sharpest gradient in the row above. This process returns the contour length of the interface. The interface length is determined by measuring the number of pixels used to outline the interface and is converted into units of length using a relation taken from the calibration images. The interface length for the interface is shown in Fig. 9 and shows that the interface length compresses initially post-reshock and then lengthens as the interface develops after reshock for Cases 1 and 2. The post-reshock interface length for Case 3 does not lengthen enough to recover from the compression caused by the reshock wave. This is a because of the well-defined structures present before reshock being compressed by the reshock wave, thus creating a region of mixed gas. The collapse of the structure eliminates the interface length associated with the structure. This inability to accurately track the interface length has been discussed by Kumar et al. (2005) who determined that once fluid began to roll up within vortex cores, the material lines could no longer be faithfully tracked, as is the case with Case 3 pre-reshock which leads to the conclusion that the post-reshock interface length measure must also not be accurate.

3.2.3 *Vorticity, circulation, and enstrophy*

The vector sets that are created by TSI INSIGHT^{TM} 4G processing can be used to take a more detailed look at the interactions present in the flow field before and after the reshock. Glycerin fog particles were used as flow tracers, the accuracy of which is detailed in the previous work of McFarland et al. (2014). The image times were selected by calculating the time necessary for the interface to travel approximately 8 pixels or 0.9144 mm (pixel size is 0.1143 mm). This conservative estimate ensures that the particles will remain within the interrogation window for the desired time interval. The pre-reshock interface velocity was calculated to be approximately 250 m/s, which yielded a delay time of 5 μs. The post-reshock velocity was calculated to be approximately 40 m/s, which yielded a delay time of approximately 25 μs. The vectors were created using a recursive Nyquist grid with a starting spot size of 36-by-36 pixels and a final spot size of 26-by-26 pixels, fast Fourier transform (FFT) correlation, and a Gaussian mask with a signal-to-noise threshold of 1.2. Holes in the vector field were filled using linear interpolation. For the pre-reshock cases, between 2 and 5 % of the vectors were interpolated, and for the post-reshock cases, between 10 and 15 % of the vectors were interpolated.

The vorticity was calculated from the curl of the 2D velocity field for all three experimental cases, and the calculated numerical derivatives produced a noisy vector field. The PIV process creates velocity vectors that are in an array based on the final spot size. The array spacing

Table 2 Interface growth rates

Case	Before or after reshock	Mixing width growth rate (m/s)	Interface length growth rate (m/s)
1	Before	29.7	44.16
	After	−83.76	15.61
2	Before	29.7	44.16
	After	−92.27	85.41
3	Before	29.7	44.16
	After	−97.75	−33.96

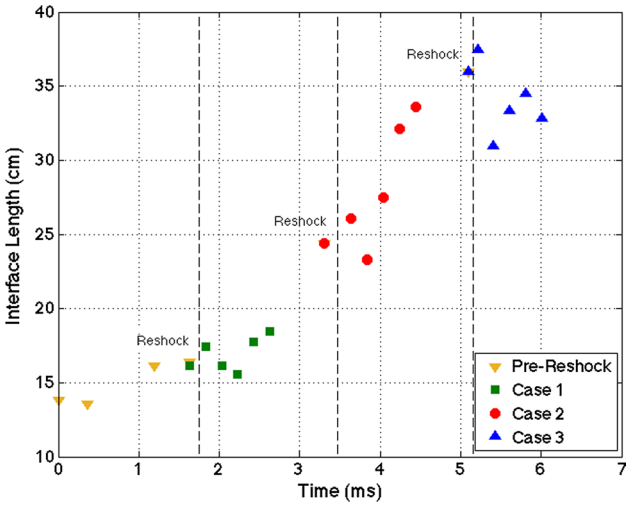

Fig. 9 Interface length plotted versus time for Cases 1, 2, and 3

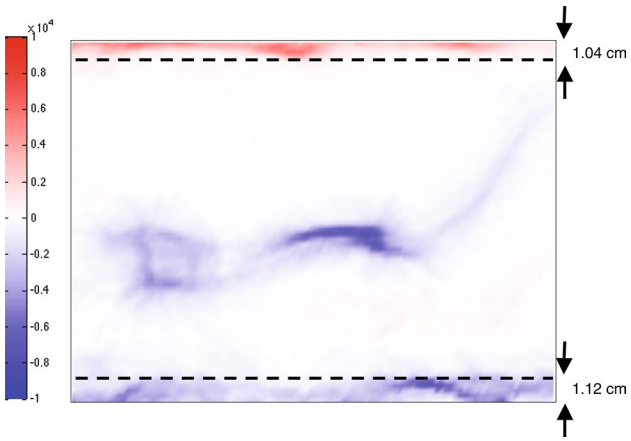

Fig. 10 A vorticity field for Case 3 pre-reshock showing the boundary layers which are cropped

can prevent gradients from being accurately represented if noise is present in the velocity vectors. To obtain more accurate derivatives, empty spaces in the vector fields were filled using linear interpolation of nearby values and then the field was smoothed using a median filter with a bin size of 11-by-11 pixels. In Fig. 10, the boundary layers are clearly identifiable in the vorticity field as layers of positive and negative vorticity. The boundary layers were cropped for all of the calculations in this work.

An example of the vector distribution acquired from the experiments along with the associated relative uncertainty is shown in Fig. 11. In this figure, the vectors are overlaid on a PLIF image for reference. The PLIF image was obtained by exciting acetone with a 266-nm laser pulse at 60 mJ. The vector resolution is one vector every 1.49 mm. Although the vectors qualitatively describe the large-scale features in this vortex structure, they do not fully capture the smaller Kelvin–Helmholtz rollups. These smaller-scale flow features will be studied in the future with a higher-resolution PIV camera. The relative uncertainty was calculated using the primary peak ratio (PPR) in TSI INSIGHT^{TM} 4G. Charonko and Vlachos (2013) correlated PIV uncertainty with image quality. The PPR, which is a ratio of the primary peak in the correlation map and the second highest peak, is a measure of image quality and is inversely related to uncertainty. The uncertainty for a 95 % confidence level was calculated using

$$|u|^2 = M \exp\left(-\frac{1}{2}\left(\frac{\mathrm{PPR}-1}{s}\right)^2\right)^2 + \left(A \cdot \mathrm{PPR}^{\beta}\right)^2 + C^2 \quad (1)$$

where M, s, A, β, and C are fitting coefficients (Charonko and Vlachos 2013). This equation models three independent sources of uncertainty, including the stated uncertainty as a function of the PPR and a Gaussian term for outliers. Xue, Charonko, and Vlachos provide an in-depth discussion of the development, use, and validation of this model using synthetic data sets (Charonko and Vlachos 2013; Xue et al. 2014). The relative uncertainty for the ensemble of ten instantaneous realizations shown in Fig. 11 varies between 5 and 15 % and is highest near the interface.

Beginning with the least temporally developed case, Case 1, the interface before reshock, as shown in Fig 12a, has no defined vortex structures but does possess many inflection points. This shape is also evident in Fig 12b where the interface is portrayed as a diffuse line of negative vorticity that is devoid of defined vortex structures, but shows stronger vorticity in areas corresponding to the inflection points of the interface. After reshock, the

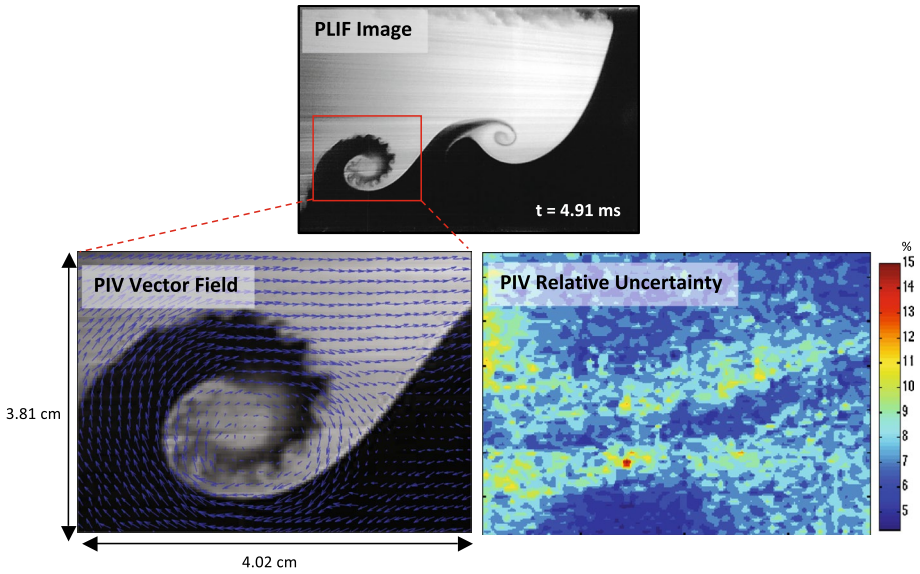

Fig. 11 A close-up view of the vortex structure in a planar laser-induced fluorescence (PLIF) image with vectors shown for Case 3 pre-reshock and associated PIV relative uncertainty calculated using the primary peak ratio (PPR)

interface is shown as a diffuse line of positive vorticity with regions of stronger vorticity which correspond to the developed structures formed from the pre-reshock inflection points. The vorticity at the interface is reversed due to the additional baroclinic torque. Furthermore, the inflections present before reshock begin to manifest themselves as small structures that can be seen in the vorticity plot post-reshock (Fig.12c).

The pre-shock vorticity plot for Case 2 shows the small vortex structure that is starting to form near the trailing edge of the interface as well as the small protrusion that is starting to extend from the interface. After the reshock interaction, the second application of baroclinic torque reverses the direction of the vorticity of the interface. This pocket of negative vorticity corresponds to the structure that was a defined vortex structure prior to reshock. Similar to the structure that is shown in the Mie scattering image in Fig. 12h, the areas of large vorticity correspond to the structures of the interface. The line of negative vorticity is also present after reshock for this case where the initial conditions are more developed.

Case 3 is the most developed pre-reshock interface and as such, has larger regions of strong vorticity within the diffuse representation of the interface. The multiple large structures in the pre-reshock interface are converted into pockets of negative vorticity by the second application of baroclinic torque and turns the bulk of the interface from negative to positive vorticity. The large areas of both negative and positive vorticity support the mixing that is inferred from the Mie scattering images.

The vorticity data collected for multiple runs for each case both before and after reshock were integrated over the flow field to determine the total enstrophy and circulation present, as shown in Table 3. The circulation is

$$\Gamma(t) = \int \int_S \vec{\omega} \cdot \mathrm{d}\vec{S}, \tag{2}$$

where $\vec{\omega}$ is vorticity and $\mathrm{d}\vec{S}$ is a differential area element.

Circulation provides an overall description of the rotational motion in the flow field at a given time and location. Circulation calculations for experiments at the same time were ensemble-averaged and compared to the standard deviation of those same experiments to obtain a measure of the repeatability. With coefficients of variance less than 7 %, the pre-reshock portion of Case 1 and Cases 2 and 3 are seen to be repeatable, while the variation of the post-reshock portion of Case 1 is quite large due to the interaction of the reflected shock, as circulation is an integral measure over the interface area.

The magnitudes of the circulation in the three cases pre-reshock are similar, and the small difference between them is because of different resolutions. The post-reshock circulation values follow a trend that the more development time allowed prior to reshock, the larger the change in circulation and magnitude of post-reshock circulation. Thus, increased development of the pre-reshock interface leads to a more complex interaction between the interface and the reshock wave which causes more circulation to be present in the flow field. In other words, there is more surface area with density gradients that result in a greater cross product upon reshock.

The enstrophy is

$$\Omega(t) = \frac{1}{2} \int \int_S \vec{\omega}^2 \cdot \mathrm{d}\vec{S}, \tag{3}$$

where $\vec{\omega}$ is vorticity and $\mathrm{d}\vec{S}$ is a differential area element. Enstrophy is a measure of the rotational energy in the flow

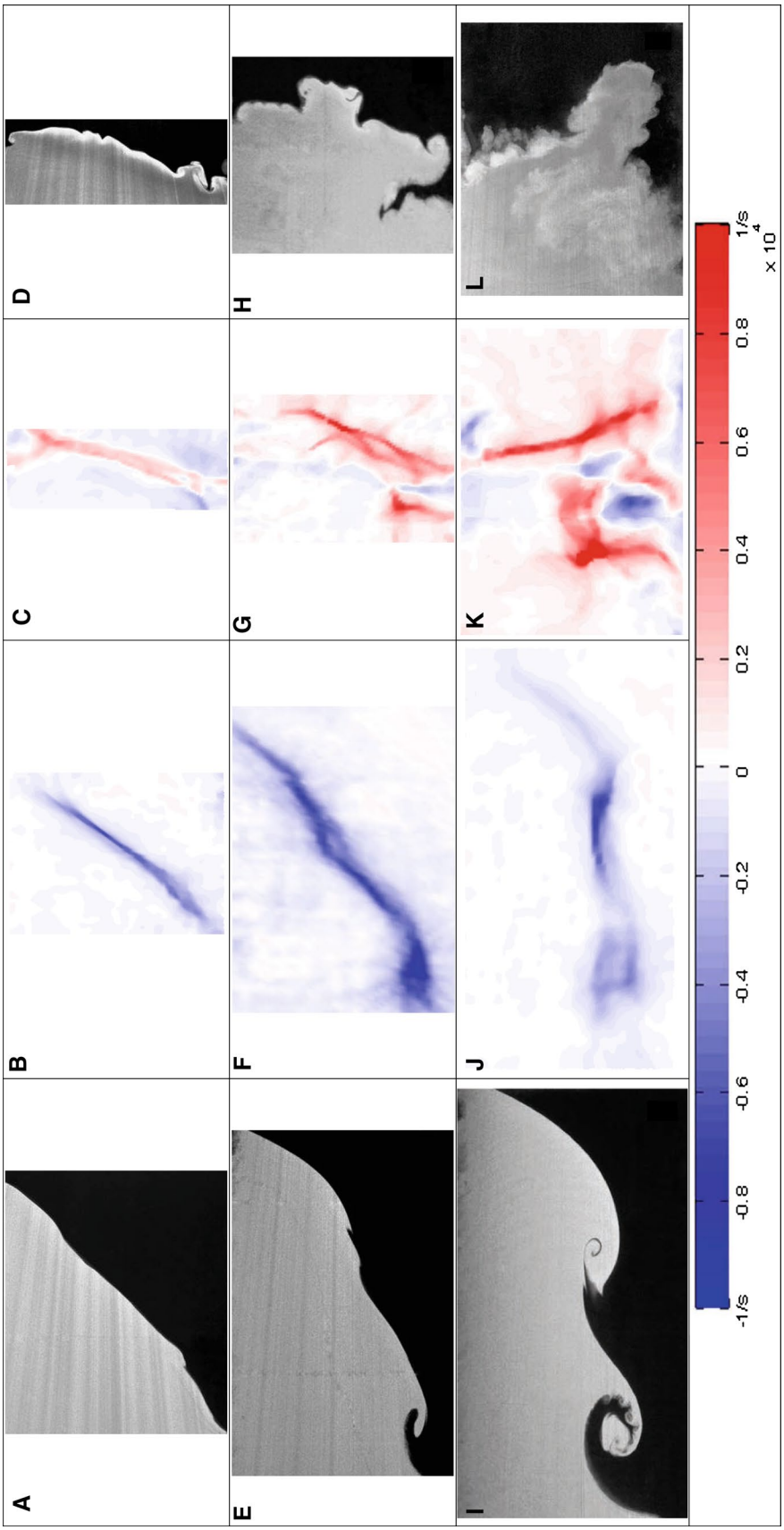

Fig. 12 Vorticity fields for the entire flow field with corresponding Mie scattering images: Case 1 before (**a**, **b**) and after (**c**, **d**) reshock interaction, Case 2 before (**e**, **f**) and after (**g**, **h**) reshock interaction, Case 3 before (**i**, **j**) and after (**k**, **l**) reshock interaction. The post-reshock times chosen were 0.64, 0.74, and 0.93 ms for Cases 1, 2, and 3, respectively

Table 3 Circulation statistics

Case	Before or after reshock	Number of experiments	Ensemble average enstrophy $(m/s)^2$	Ensemble average circulation (m^2/s)	Standard deviation (m^2/s)	Coefficient of variance (%)
1	Before	10	6.27×10^{-3}	−3.218	0.119	3.71
	After	10	6.81×10^{-3}	3.893	0.307	7.88
2	Before	8	6.83×10^{-3}	−3.845	0.147	3.82
	After	10	1.83×10^{-2}	7.246	0.283	3.91
3	Before	9	1.214×10^{-2}	−3.742	0.212	5.66
	After	8	3.55×10^{-2}	8.862	0.312	3.52

field at a given time and location. Enstrophy calculations for experiments at the same time were ensemble-averaged.

The enstrophy across the reshock interaction for all cases increases which shows that there is more local rotation occurring in the post-reshock flow fields. As the large, coherent structures of the interface break down during the post-reshock development and smaller-scale structures develop, the rotational motion of the flow is enhanced locally as it is dissipated from the larger scales. Case 1 has fewer coherent structures than the other cases post-reshock, and therefore, its post-reshock enstrophy is found to be less than that of Cases 2 and 3. As expected, Case 3 is found to have more post-reshock enstrophy than Case 2.

3.2.4 Velocity statistics

Important to understanding turbulent flows are Reynolds stresses or turbulent stresses which depend on velocity fluctuations, both streamwise and spanwise, and account for turbulent fluctuations in fluid momentum. The Reynolds stresses in a Richtmyer–Meshkov fluid mixing layer were recently studied by Balakumar et al. (2012). The streamwise velocity fluctuation is defined as

$$u' = u - \overline{u} \tag{4}$$

where u is the streamwise velocity and $\overline{u}$ is the spatially averaged streamwise velocity. The spanwise velocity fluctuation definition is of the same form.

The variation in streamwise and spanwise velocity fluctuations was plotted across the mixing width for each case before and after reshock (Fig. 13). All of the variances were ensemble-averaged over ten instantaneous realizations (i.e., separate experiments). The streamwise velocity variance pre-reshock is an order of magnitude larger than the spanwise velocity variance, which indicates that there is anisotropy present in the flow field in the direction of shock propagation. The nonzero cross-correlation ($\overline{u'v'}$) between the streamwise and spanwise velocity fluctuations indicates that there is shear present in the flow which leads to the Kelvin–Helmholtz rollups visible in the Mie scattering images. Furthermore, in Case 3 pre-reshock there is a bimodal distribution in $\overline{u'^2}$ due to the two vortex structures that form. There is a trend of increasing streamwise velocity fluctuation variance from Case 1 to Case 3. Moreover, the streamwise velocity fluctuation variance increases by a factor of four after reshock for Cases 2 and 3, but remains nearly unchanged for Case 1. For the most developed case, Case 3, the maximum streamwise velocity fluctuation before reshock is ~7 % of the bulk fluid velocity.

3.2.5 Turbulent kinetic energy spectra

An approximation of the turbulent kinetic energy (TKE) spectrum using available 2D data was used to quantify the scales over which energy is distributed. The method used to calculate the spectra presented in this work is similar to the method used by Latini et al. (2007) with the exception that density weighting was not employed. First, vorticity plots for each case were examined and the boundary layers (clearly visible in the vorticity plot) were cropped. Because only half of a wavelength is studied in the inclined shock tube, as shown in Fig. 7, the PIV data were reflected across the bottom, horizontal boundary (the floor of the shock tube). This resulted in one full wavelength, which is periodic when taking the Fourier transform. The u' and v' components of turbulent kinetic energy are given by

$$K_{u'} = \frac{1}{2}\overline{u'^2} \tag{5}$$

$$K_{v'} = \frac{1}{2}\overline{v'^2} \tag{6}$$

where u' and v' are the streamwise and spanwise components of the fluctuating velocities, respectively. The energy spectra components were computed by taking the FFT of each column of fluctuating velocities in the spanwise direction and multiplying it by its complex conjugate

$$[E_{u'}]_i = \mathrm{FFT}(u') \cdot \mathrm{conj}(\mathrm{FFT}(u')) \tag{7}$$

$$[E_{v'}]_i = \mathrm{FFT}(v') \cdot \mathrm{conj}(\mathrm{FFT}(v')) \tag{8}$$

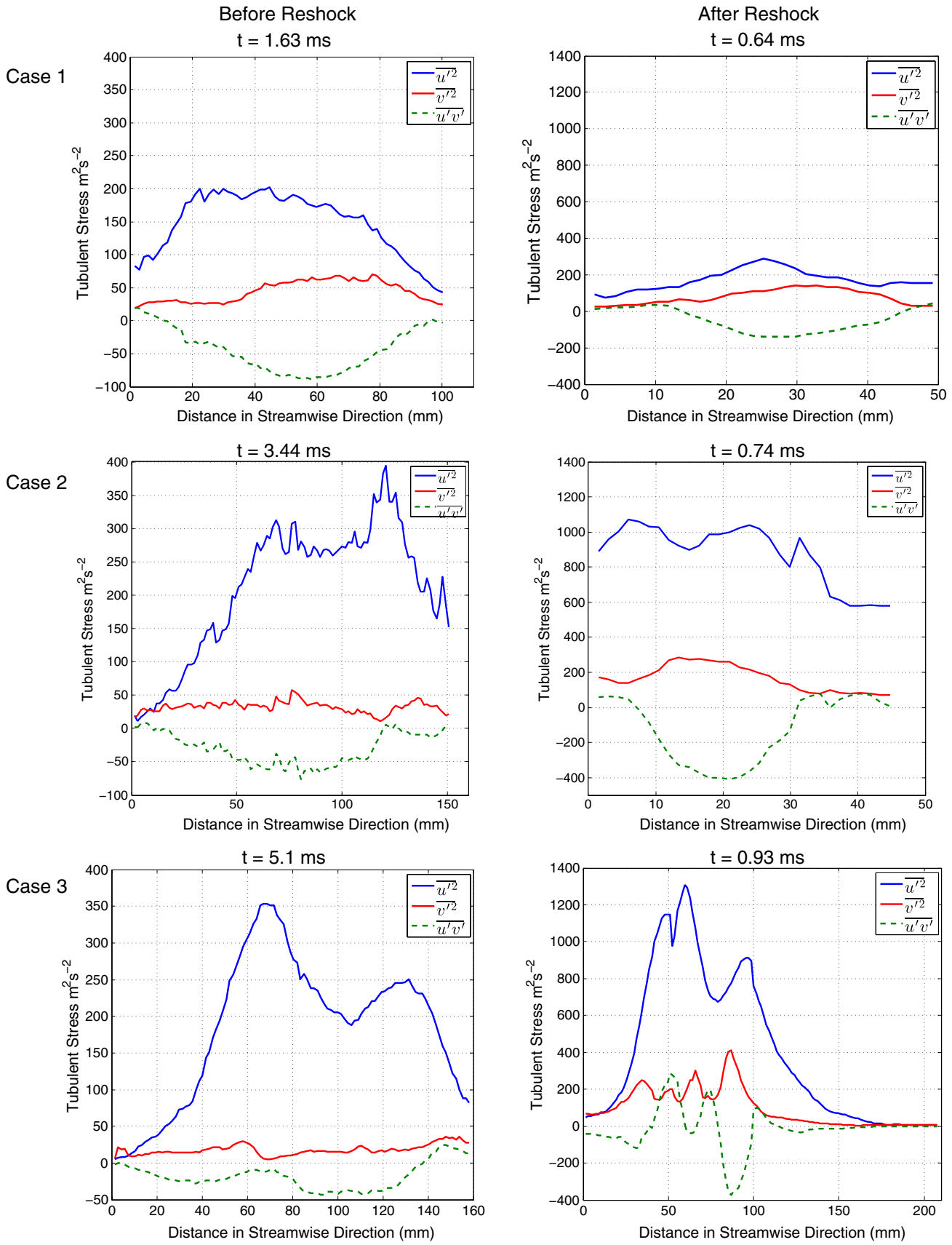

Fig. 13 Variances of velocity fluctuations across the mixing width in the streamwise direction before and after reshock interaction for Cases 1, 2, and 3 (the post-reshock times are relative to when reshock happens, whereas the pre-reshock times are relative to the incident shock time)

where $[E_{u'}]_i$ is the u' component of the energy spectra for the ith column. The energy spectra were calculated by adding the u' and v' components.

$$[E]_i = \frac{1}{2}[[E_{u'}]_i + [E_{v'}]_i] \tag{9}$$

After the energy spectra were averaged across all the columns, only the first half was retained due to the Nyquist sampling frequency restraint. This procedure was performed on approximately ten instantaneous realizations for each case; thus, the overall average used 4340 columns of velocity data, including mirrored ones.

The spectra for the experimental data sets are shown in Fig. 14. In the majority of cases, the spectra show two decades of spread at small wavenumbers but collapse at wavenumbers larger than 1000 m^{-1}. A large amount of energy is present at low wavenumbers because of the large length scale of the inclined-interface perturbation.

In order to better understand the spectra, the Kolmogorov scale and the Taylor microscale were calculated. The Kolmogorov length scale is approximately equal to the product of the largest length scale λ_k and the Reynolds number to the −3/4 power

$$\lambda_k \approx hRe^{-3/4} \tag{10}$$

where h is the largest length scale and Re is the Reynolds number. The largest length scale is the mixing width defined by the 5 and 95 % mole fractions of the constituent gases. The Kolmogorov length scale gives an estimate of the high-wavenumber end of the inertial subrange. Furthermore, the Reynolds number is

$$Re = \frac{h\dot{h}}{\nu_{\text{mix}}} \tag{11}$$

where $\dot{h}$ is the interface growth rate, h is the mixing width, and $\nu_{\text{mix}} = \frac{\mu_1+\mu_2}{\rho_1+\rho_2}$ is the kinematic viscosity of the mixture of gases. The kinematic mixture viscosity before and after reshock was calculated using one-dimensional gas dynamics and property relations to be 6.27×10^{-6} and 4.08×10^{-6} Pa s, respectively. Also, the mixing width growth rates come from the center column from Table 2. Just after reshock for Case 3, the Reynolds number was calculated to be 2.16×10^6. It follows that the Kolmogorov length scale is on the order of 10^{-6} m, which is three orders of magnitude below the PIV resolution. Dimotakis (2000) argues that a necessary condition for a transition to turbulence is a Reynolds number of ∼1–2 × 10^4, so all of the cases discussed here have the potential to be in the turbulent regime. Another useful length scale is the Taylor microscale ($\lambda_L \approx \sqrt{15}hRe^{-1/2}$), which gives an estimate of the largest scales which are isotropic and independent of large-scale features in the flow field Robey et al. (2003). In other words, the Taylor microscale indicates the low-wavenumber end of the inertial subrange predicted by Kolmogorov. The values for the Kolmogorov scale and Taylor microscale for Case 3 post-reshock calculated using both the interface growth rate (based on mixing width) and circulation (Γ/ν_{mix}) are presented in Table 4. The circulation-based calculations compare well with the growth-rate-based ones. The Taylor microscale is one order of magnitude below the PIV resolution. Higher-resolution CCD cameras will be implemented in future experiments to capture more of these scales.

Figure 15 compares the average spectra for all three cases before and after reshock. In all cases, the reshock wave causes an amplification of turbulent kinetic energy which is seen at all wavenumbers. Cases 2 and 3 TKE is amplified by approximately one order of magnitude. WENO simulations (Schilling and Latini 2010) of a 3D reshocked RMI also showed approximately one decade of amplification of TKE upon reshock. Case 1 has a much smaller increase in TKE because fewer small scales have formed. Cases 1 and 2 pre-reshock begin to follow a $k^{-5/3}$ power law for a small range of wavenumbers, whereas Case 3 pre-reshock follows this trend for a larger range. As the interface is given a longer time to develop prior to reshock, it approaches a turbulent state. The complexity of the Case 3 interface leads to a redistribution of energy over a large range of scales upon reshock. After reshock, all three cases follow a $k^{-5/3}$ power law for a larger range of wavenumbers, with Case 3 following this trend for the largest range (approximately one decade). This trend indicates that energy contained at large wavenumbers is converging toward an isotropic state (Ramaprabhu and Andrews 2004). The sharp decline at the highest wavenumbers is due to aliasing effects. Energy in the dissipation range cannot be measured here due to limitations in PIV resolution.

4 Conclusions

From the Mie scattering image time series for Cases 1, 2, and 3, it can be determined that a more developed pre-reshock interface results in a more mixed post-reshock interface. Although the mixing width decreases after reshock, the interface length continues to increase because the reshock wave amplifies small-scale perturbations on the pre-reshock interface. Although the same amount of energy is deposited by the first shock for all three cases, there are different amounts of energy deposited by the second shock (reshock). The more developed the interface, the more energy is deposited by reshock due to the larger surface area with a density gradient, which provides a larger $\vec{\nabla}\rho \times \vec{\nabla}P$. The most developed interface also receives more vorticity deposition. After reshock, the sign of the vorticity near the interface changes because of the additional

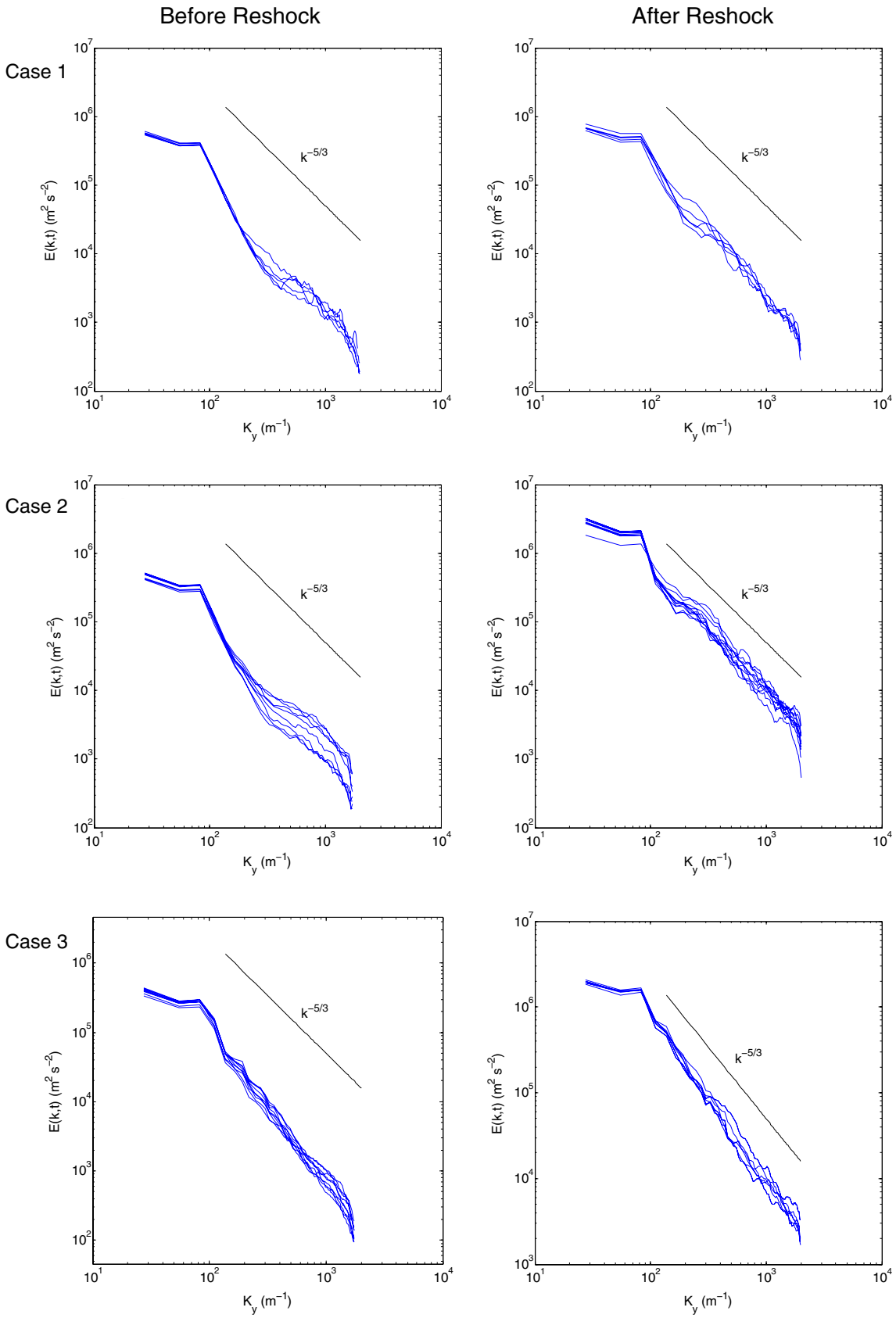

Fig. 14 Ensemble of approximate turbulent kinetic energy spectra for each case for before and after reshock interaction for Cases 1, 2, and 3

Table 4 Reynolds numbers and Kolmogorov and Taylor scales for case 3 after reshock

Case	Calculation method	Time (ms)	Reynolds number	Kolmogorov scale (μm)	Taylor microscale (μm)
3	Interface growth-rate-based Reynolds number	0.93	2.16×10^6	1.60	237.41
	Circulation-based Reynolds number	0.93	2.17×10^6	1.59	236.62

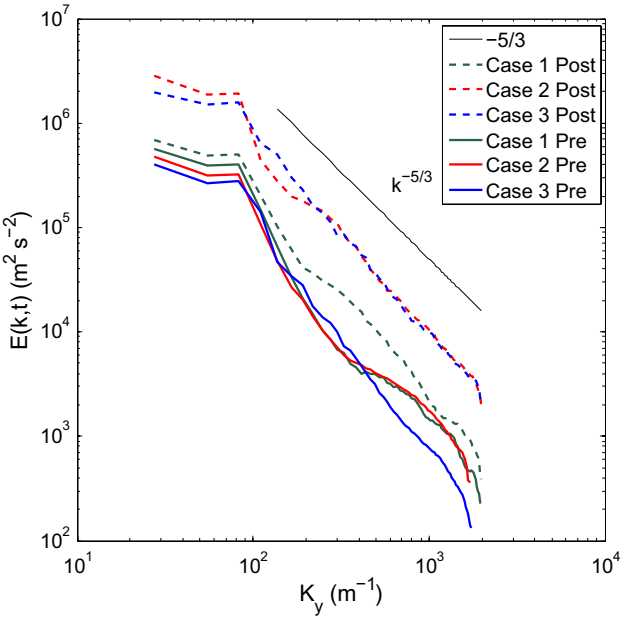

Fig. 15 Ensemble-averaged approximate turbulent kinetic energy spectra for all three cases for before and after reshock with $k^{-5/3}$ fiducial

baroclinic torque applied by the reshock wave. Velocity statistics show that the cross-correlation ($\overline{u'v'}$) is nonzero over much of the mixing layer, which means that there is shear and anisotropy present. All three cases begin to develop an inertial range after reshock, but only Case 3 begins to develop this range before reshock. Case 3's vorticity is better distributed compared to the other two cases, which is why it develops an inertial range faster and follows a $k^{-5/3}$ power law longer.

Acknowledgments The authors are grateful to Skylar Creel for helping with the experiments. This work was partially supported by the National Science Foundation Faculty Early Career Development (CAREER) Award (Award No. 1451994).

References

Abd-El-Fattah A, Henderson L (1978) Shock waves at a fast-slow gas interface. J Fluid Mech 86:15–32

Abd-El-Fattah A, Henderson L (1978) Shock waves at a slow-fast gas interface. J Fluid Mech 89:79–95

Abd-El-Fattah A, Henderson LF, Lozzi A (1976) Precursor shock waves at a slow-fast gas interface. J Fluid Mech 76:157–176

A. T. plc Working Instruction (1998) Particle size calibration of high output aerosol generators

Balakumar B, Orlicz G, Tomkins C, Prestridge K (2008) Simultaneous particle-image velocimetry-planar laser-induced fuorescence measurements of Richtmyer–Meshkov instability growth in a gas curtain with and without reshock. Phys Fluids 20:124103

Balakumar B, Orlicz G, Ristorcelli J, Balasubramanian S, Prestridge K, Tomkins C (2012) Turbulent mixing in a Richtmyer–Meshkov fluid layer after reshock: velocity and density statistics. J Fluid Mech 696:67–93

Chapman P, Jacobs J (2006) Experiments on the three-dimensional incompressible Richtmyer–Meshkov instability. Phys Fluids 18:074101

Charonko JJ, Vlachos PP (2013) Estimation of uncertainty bounds for individual particle image velocimetry measurements from cross-correlation peak ratio. Meas Sci Technol 24:065301

Dimotakis PE (2000) The mixing transition in turbulent ows. J Fluid Mech 409:69–98

Hill D, Pantano C, Pullin D (2006) Large-eddy simulation and multiscale modelling of a Richtmyer–Meshkov instability with reshock. J Fluid Mech 557:29–62

Jahn RG (1956) The refraction of shock waves at a gaseous interface. J Fluid Mech 1:457–489

Jones M, Jacobs J (1997) A membraneless experiment for the study of Richtmyer–Meshkov instability of a shock-accelerated gas interface. Phys Fluids 9:3078

Kramer KJ, Latkowski JF, Abbott RP, Boyd JK, Powers JJ, Seifried JE (2009) Neutron transport and nuclear burnup analysis for the laser inertial confinement fusion-fission energy (life) engine. Fusion Sci Technol 56:625

Kumar S, Orlicz G, Tomkins C, Goodenough C, Prestridge K, Vorobieff P, Benjamin R (2005) Stretching of material lines in shock-accelerated gaseous ows. Phys Fluids (1994-present) 17:082107

Latini M, Schilling O, Don WS (2007) Effects of WENO flux reconstruction order and spatial resolution on reshocked two-dimensional Richtmyer–Meshkov instability. J Comput Phys 221:805–836

Leinov E, Malamud G, Elbaz Y, Levin L, Ben-Dor G, Shvarts D, Sadot O (2009) Experimental and numerical investigation of the Richtmyer–Meshkov instability under re-shock conditions. J Fluid Mech 626:449

McFarland JA, Greenough JA, Ranjan D (2011) Computational parametric study of a Richtmyer–Meshkov instability for an inclined interface. Phys Rev E 84:026303

McFarland JA, Greenough JA, Ranjan D (2014) Simulations and analysis of the reshocked inclined interface Richtmyer–Meshkov instability for linear and nonlinear inter- face perturbations. J Fluids Eng 136:071203

McFarland J, Reilly D, Creel S, McDonald C, Finn T, Ranjan D (2014) Experimental investigation of the inclined interface Richtmyer–Meshkov instability before and after reshock. Exp Fluids 55:1–14

Meshkov E (1969) Instability of the interface of two gases accelerated by a shock wave. Fluid Dyn. 4:101–104

Morgan RV, Aure R, Stockero JD, Greenough JA, Cabot W, Likhachev OA, Jacobs JW (2012) On the late-time growth of the

two-dimensional Richtmyer–Meshkov instability in shock tube experiments. J Fluid Mech 712:354–383

Olmstead D, Truman C, Wayne P, Vorobieff P (2015) Effects of inclination angle on a shock-accelerated heavy gas column. Comput Methods Multiph Flow VIII 89:171

Peng G, Zabusky NJ, Zhang S (2003) Vortex-accelerated secondary baroclinic vorticity deposition and late-intermediate time dynamics of a two-dimensional Richtmyer–Meshkov interface. Phys Fluids 15:3730–3744

Ramaprabhu P, Andrews M (2004) Experimental investigation of Rayleigh–Taylor mixing at small Atwood numbers. J Fluid Mech 502:233–271

Richtmyer RD (1960) Taylor instability in shock acceleration of compressible fluids. Commun Pure Appl Math 13:297–319

Robey H, Zhou Y, Buckingham A, Keiter P, Remington B, Drake R (2003) The time scale for the transition to turbulence in a high reynolds number, accelerated ow. Phys Plasmas 10:614

Samtaney R, Zabusky NJ (1993) On shock polar analysis and analytical expressions for vorticity deposition in shock-accelerated density-stratified interfaces. Phys Fluids A Fluid Dyn 5:1285

Schilling O, Latini M (2010) High-order WENO simulations of three-dimensional reshocked Richtmyer–Meshkov instability to late times: dynamics, dependence on initial conditions, and comparisons to experimental data. Acta Math Sci 30:595–620

Schilling O, Latini M, Don WS (2007) Physics of reshock and mixing in single-mode Richtmyer–Meshkov instability. Phys Rev E 76:026319

Smith A, Holder D, Barton C, Morris A, Youngs D (2001) Shock tube experiments on Richtmyer–Meshkov instability across a chevron profiled interface. In: Proceedings of the eighth international workshop on the physics of compressible turbulent mixing

Vetter M, Sturtevant B (1995) Experiments on the Richtmyer–Meshkov instability of an air/SF6 interface. Shock Waves 4:247–252

Wayne P, Olmstead D, Truman CR, Vorobieff P, Kumar S (2015) Oblique shock interaction with a laminar cylindrical jet. Bull Am Phys Soc 60. http://meetings.aps.org/link/BAPS.2015.SHOCK.H4.4

Xue Z, Charonko JJ, Vlachos PP (2014) Particle image velocimetry correlation signal-to-noise ratio metrics and measurement uncertainty quantification. Meas Sci Technol 25:115301